

On the settling depth of meltwater escaping from beneath Antarctic ice

shelves

Constantin W. Arnscheidt* and John Marshall

Department of Earth, Atmospheric, and Planetary Sciences, Massachusetts Institute of Technology, Cambridge, MA, USA

Pierre Dutrieux

British Antarctic Survey, Natural Environment Research Council, Cambridge, UK and Lamont-Doherty Earth Observatory of Columbia University, Palisades, NY, USA

Craig D. Rye

Department of Earth, Atmospheric, and Planetary Sciences, Massachusetts Institute of Technology, Cambridge, MA, USA and Goddard Institute for Space Studies, New York City, NY, USA

Ali Ramadhan

Department of Earth, Atmospheric, and Planetary Sciences, Massachusetts Institute of Technology, Cambridge, MA, USA

*Corresponding author: Constantin W. Arnscheidt, cwa@mit.edu

ABSTRACT

17 Antarctic glacial meltwater is thought to play an important role in determining large-scale Southern
18 Ocean climate trends, yet recent modeling efforts have proceeded without a good understanding
19 of how its vertical distribution in the water column is set. To rectify this, here we conduct new
20 large-eddy simulations of the ascent of a buoyant meltwater plume after its escape from beneath
21 an Antarctic ice shelf. We find that the meltwater's settling depth is primarily a function of the
22 buoyancy forcing per unit width of the source and the ambient stratification, consistent with the
23 classical theory of turbulent buoyant plumes and in contrast to previous work that suggested an
24 important role for centrifugal instability. Our results further highlight the significant role played
25 by localized variability in stratification; this helps explain observed interannual variability in the
26 vertical meltwater distribution near Pine Island Glacier. Because of the vast heterogeneity in mass
27 loss rates and ambient conditions at different Antarctic ice shelves, a dynamic parameterization
28 of meltwater settling depth may be crucial for accurately simulating high-latitude climate in a
29 warming world; we discuss how this may be developed following this work, and where the
30 remaining challenges lie.

31 **1. Introduction**

32 A notable failure of the global coupled climate models included in the Coupled Model
33 Intercomparison Project Phase 5 (CMIP5, Taylor et al. 2012) has been their inability to hindcast
34 important observed Southern Ocean climate trends such as surface cooling, surface freshening,
35 and sea-ice expansion (Turner et al. 2013; Jones et al. 2016; Kostov et al. 2018). Recent work
36 suggests that the increase in the Antarctic meltwater anomaly over this period may have played an
37 important role in driving the observed trends (Rye et al. 2020). Climate models typically neglect
38 the anomalous freshwater flux due to net mass loss from the Antarctic ice sheet: this has increased
39 over the past few decades to around 500 Gt/yr (Paolo et al. 2015; Rignot et al. 2019). Recent work
40 suggests that the incorporation of this meltwater anomaly into climate models could help to explain
41 the observed trends, resolving the discrepancy between observations and simulations (Bintanja
42 et al. 2013; Rye et al. 2014; Bintanja et al. 2015; Rye et al. 2020). The incorporation of Antarctic
43 glacial meltwater also has a significant impact on projections of future climate (Bronselaer et al.
44 2018; Golledge et al. 2019). Although there remains some disagreement about the magnitude of
45 the climate impacts due to meltwater (Swart and Fyfe 2013; Pauling et al. 2016), understanding
46 how to correctly represent this process in global climate models is clearly of importance.

47 In climate modeling studies, the meltwater has generally been represented as an externally
48 imposed freshwater flux; this requires a starting assumption about where in the water column the
49 glacial meltwater is situated. In many studies, glacial meltwater has been introduced at or near the
50 surface (Bintanja et al. 2013; Swart and Fyfe 2013; Rye et al. 2014; Bintanja et al. 2015; Hansen
51 et al. 2016; Pauling et al. 2016; Bronselaer et al. 2018), or over a constant depth (Rye et al. 2020).
52 Even though most of the melting occurs at depth, the meltwater might be expected to rise to the
53 surface due to its relatively low density; however, this assumption is not supported by observations.

54 For example, measurements of noble gas concentrations in the Ross Sea (Loose et al. 2009) and
55 in the Amundsen Sea (Kim et al. 2016; Biddle et al. 2019) reveal vertical meltwater distributions
56 centered at around 300m-400m depth. Near Pine Island Glacier, which is the source of a large
57 fraction of the total Antarctic melt, Dutrieux et al. (2014b) found a large interannual variability in
58 meltwater settling depth, with meltwater settling close to the surface in some years and hundreds
59 of meters at depth in other years. A better understanding of what determines the settling depth
60 of Antarctic glacial meltwater may greatly improve our understanding of ice-ocean interactions as
61 well as their representation in climate models.

62 Aspects of glacial meltwater dynamics have been studied previously. In the Antarctic context,
63 the priority has been to determine the rate and spatial distribution of sub-ice-shelf melting for
64 given boundary conditions and forcings. To this end, studies have employed plume models in
65 one (MacAyeal 1985; Jenkins 1991, 2011; Lazeroms et al. 2018) and two (Holland et al. 2007)
66 dimensions, box models (Olbers and Hellmer 2010; Reese et al. 2018), and three-dimensional fluid
67 dynamics simulations on the ice-shelf scale (Losch 2008; De Rydt et al. 2014; Mathiot et al. 2017).
68 In an Arctic context, where meltwater is generally released from near-vertical tidewater glaciers at
69 the ends of enclosed fjords instead of from underneath an ice shelf cavity, meltwater plumes have
70 been studied using both one-dimensional plume theory and high-resolution numerical simulations
71 (Xu et al. 2012, 2013; Sciascia et al. 2013; Kimura et al. 2014; Carroll et al. 2015; Cowton
72 et al. 2015; Slater et al. 2015, 2016; Ezhova et al. 2018). Finally, Naveira Garabato et al. (2017)
73 have studied the small-scale (10-100m) fluid dynamics of meltwater escaping from underneath an
74 Antarctic ice shelf, with an explicit focus on meltwater settling depth. They simulated the evolution
75 of a meltwater plume in a two-dimensional plane perpendicular to the ice-shelf front, and argued
76 that centrifugal instability, through its effect on lateral mixing, plays a dominant role in controlling
77 the settling depth.

78 In this study, we revisit the small-scale fluid dynamics of meltwater ascent along an ice-shelf
79 front after its escape from within the cavity. First, we describe an idealized meltwater ascent
80 scenario, and introduce simple models for the meltwater's settling depth. Second, we describe
81 new three-dimensional large-eddy simulations of the meltwater plume, and compare the results to
82 the predictions of the simpler models. Third, we use our models to address observed interannual
83 variability in meltwater settling depth near Pine Island Glacier. Finally, we discuss why a dynamic
84 parameterization of meltwater settling depth could be crucial for accurately simulating high-latitude
85 climate, and outline how such a parameterization could be implemented building in part on the
86 work in this study.

87 2. Theory and Methods

88 The object of this study is described schematically in Figure 1. Much of the total mass loss from
89 the Antarctic ice sheet stems from a small number of rapidly-melting ice shelves; here, we focus
90 on Pine Island Glacier, which is the source of a large fraction of the total mass loss (Rignot et al.
91 2019). The meltwater outflow from underneath the Pine Island ice shelf is concentrated in a narrow
92 km-scale flow at its western edge (Thurnherr et al. 2014; Naveira Garabato et al. 2017). A similarly
93 narrow meltwater outflow may be a feature of many Antarctic ice shelves, as it is a consequence
94 of a typical sub-ice-shelf circulation (e.g. Grosfeld et al. 1997; Losch 2008). We investigate the
95 dynamics of such a meltwater outflow by idealizing it as a prescribed, constant buoyancy source
96 F , with width L , applied to the bottom of our model domain. In the real world, this buoyancy
97 source is a function of complex melting and mixing processes beneath the ice shelf cavity; explicit
98 consideration of these is beyond the scope of this paper. In this section, we outline the hierarchy
99 of theoretical and modeling approaches that we will use.

¹⁰⁰ a. Simple scaling relationships

¹⁰¹ The glacial meltwater escaping from underneath the ice shelf undergoes turbulent buoyant
¹⁰² convection in a stratified ambient fluid. The theory of such processes was first developed by Morton
¹⁰³ et al. (1956). For plumes originating from a point source, far from any walls, this theory has yielded
¹⁰⁴ robust scaling laws for the plume's rise height in terms of the buoyancy source F and the ambient
¹⁰⁵ stratification N . These scaling laws have been repeatedly confirmed in laboratory and experimental
¹⁰⁶ work (Turner 1986; Helfrich and Battisti 1991; Speer and Marshall 1995; Fabregat Tomàs et al.
¹⁰⁷ 2016). As described, for example, by Speer and Marshall (1995), as long as N is substantially
¹⁰⁸ larger than the Coriolis parameter f , the only two parameters that could physically control the rise
¹⁰⁹ height are F (m^4/s^3 , consider an area-integrated buoyancy flux) and N (s^{-1}). Assuming both terms
¹¹⁰ to be constant, dimensional analysis then yields a vertical scale

$$h_N = \left(\frac{F}{N^3} \right)^{\frac{1}{4}}. \quad (1)$$

¹¹¹ The real rise height h is proportional to this vertical scale:

$$h = ah_N, \quad (2)$$

¹¹² where a is a constant. Numerical experiments consistently yield a value of $a \simeq 2.6$ (e.g. Speer and
¹¹³ Marshall 1995; Fabregat Tomàs et al. 2016).

¹¹⁴ In the case of the glacial meltwater outflow, however, the meltwater plume does not originate
¹¹⁵ from a point source: it is rather in the shape of a line, where the total buoyancy forcing F is
¹¹⁶ distributed over some width L (see Figure 1). Therefore, we modify equation (1) by assuming that
¹¹⁷ the two parameters exerting control over the rise height are the buoyancy source per unit width,
¹¹⁸ F/L (m^3/s^3), and the ambient stratification, N (s^{-1}). Dimensional analysis now yields a vertical

₁₁₉ scale of

$$h_N = \left(\frac{F}{L}\right)^{\frac{1}{3}} \frac{1}{N}. \quad (3)$$

₁₂₀ Again, the real rise height is proportional to this scale:

$$h = ah_N. \quad (4)$$

₁₂₁ The constant of proportionality here could naively be expected to match the value observed for
₁₂₂ plumes originating from a point source ($a \approx 2.6$), and the simulations we conduct in this study
₁₂₃ indeed confirm that it does (Section 3b).

₁₂₄ We emphasize that the buoyancy forcing F/L is an abstraction. In the real world, the effective
₁₂₅ buoyancy flux escaping from underneath the ice shelf is a complex function of the meltwater
₁₂₆ dynamics within the cavity. For example, F/L depends on the total melting within the cavity, on
₁₂₇ the spatial distribution of melting (because buoyant meltwater parcels released at depth will lose
₁₂₈ buoyancy on their ascent towards the ice-shelf front), and on the mixing with ambient cavity water.
₁₂₉ It also depends on the nature of the sub-ice-shelf circulation, and to what extent this focuses the
₁₃₀ outflow into a narrow jet as is the case for the Pine Island ice shelf. While F/L could in principle
₁₃₁ be calculated using a sufficiently sophisticated sub-ice-shelf model, our approach in this study will
₁₃₂ be to treat it primarily as a tunable parameter. This will allow us to gain an understanding of the
₁₃₃ ice-shelf-front-adjacent meltwater dynamics corresponding to a wide range of sub-ice-shelf melt
₁₃₄ scenarios.

₁₃₅ *b. One-dimensional line plume model*

₁₃₆ The scaling theory described above cannot account for the effects of non-uniform stratification
₁₃₇ (i.e. $N = N(z)$), and provides only limited physical insight. To improve upon it, we follow Morton
₁₃₈ et al. (1956) in constructing a one-dimensional vertical steady-state model of the buoyant plume.

139 The original model of Morton et al. (1956) describes a point buoyancy source, and has been
 140 previously adapted to consider a point source of meltwater next to a vertical wall (Cowton et al.
 141 2015; Carroll et al. 2015; Ezhova et al. 2018). One-dimensional models of buoyant line plumes
 142 rising underneath a sloping interface have also been widely applied to the study of sub-ice-shelf
 143 meltwater dynamics (MacAyeal 1985; Jenkins 1991, 2011; Lazeroms et al. 2018; Pelle et al. 2019).
 144 These models generally consider explicit fluxes of heat and salt instead of a generic buoyancy flux,
 145 as well as interactions across the ice-ocean interface.

146 Throughout this study we will assume that the dominant contribution to meltwater production is
 147 made below the ice shelf and that thermodynamic interactions between the plume and the ice shelf
 148 front itself (see Figure 1) are negligible. For a buoyant plume originating from a line source next
 149 to a vertical wall, these assumptions lead to the following system of coupled ordinary differential
 150 equations (see Appendix A):

$$\frac{dQ}{dz} = \alpha \frac{M}{Q} \quad (5)$$

$$\frac{dM}{dz} = \frac{QB}{M} \quad (6)$$

$$\frac{dB}{dz} = -QN^2. \quad (7)$$

151 Here Q , M , and B are vertical fluxes per unit length of volume, momentum, and buoyancy,
 152 respectively. $N(z)$ is the ambient stratification, and α is a non-dimensional entrainment coefficient.
 153 The model is solved for a given buoyancy forcing F/L by setting $B = F/L$ at the bottom of the
 154 domain and integrating upwards. The meltwater's settling depth is then given by the level of neutral
 155 buoyancy, which is where $B(z) = 0$. Since F/L and N are the only dimensional input parameters,
 156 a characteristic vertical scale is again given by $h_N = (F/L)^{1/3}/N$.

157 Example solutions of this one-dimensional model are shown in Figure 2, for a range of buoyancy
 158 forcings F/L . Here, the ambient stratification $N = 3 \times 10^{-3} \text{ s}^{-1}$, a realistic value for Pine Island Bay.

₁₆₁ Values used for the entrainment coefficient vary across the literature; here, we use $\alpha = 0.15$, which
₁₆₂ is consistent with effective entrainment coefficients calculated from past numerical simulations of
₁₆₃ hydrothermal plumes (Jiang and Breier 2014; Fabregat Tomàs et al. 2016). We integrate our model
₁₆₄ equations using an eighth-order Runge-Kutta method (Prince and Dormand 1981).

₁₆₅ *c. Three-dimensional large-eddy simulations*

₁₆₆ To accurately study the behavior of the buoyant plume, and to evaluate the utility of the simpler
₁₆₇ theories described above, we conduct high-resolution simulations of the underlying small-scale
₁₆₈ fluid dynamics. Many previous studies have simulated the dynamics of geophysical plumes
₁₆₉ rising far from any walls (e.g. Lavelle 1995; Speer and Marshall 1995; Jiang and Breier 2014;
₁₇₀ Fabregat Tomàs et al. 2016). In the Arctic context, past studies have simulated glacial meltwater
₁₇₁ plumes rising next to a wall (Xu et al. 2012, 2013; Sciascia et al. 2013; Kimura et al. 2014; Carroll
₁₇₂ et al. 2015; Slater et al. 2015; Ezhova et al. 2018); the results are generally consistent with buoyant
₁₇₃ plume theory as long as the meltwater contribution from the ice face is small. However, it is unclear
₁₇₄ to what extent this is true of Antarctic meltwater plumes. Aside from the difference in geometry
₁₇₅ between these two contexts, studies of Arctic meltwater plumes typically neglect the effects of the
₁₇₆ Earth's rotation, which in principle can have a substantial effect on settling depth (Fabregat Tomàs
₁₇₇ et al. 2016). While neglecting rotation may be reasonable within Greenlandic fjords (e.g. Straneo
₁₇₈ et al. 2010; Sciascia et al. 2013), it is not reasonable for meltwater escaping from beneath Antarctic
₁₇₉ ice shelves. For example, Naveira Garabato et al. (2017) showed using observations and two-
₁₈₀ dimensional simulations that the Coriolis force is responsible for a vigorous zonal jet next to the
₁₈₁ meltwater outflow from underneath the Pine Island ice shelf. They further argued that rotation
₁₈₂ had an important effect on the meltwater's settling depth, through the mechanism of centrifugal
₁₈₃ instability.

184 The vast majority of these numerical simulations of glacial meltwater plumes have used the
185 Massachusetts Institute of Technology general circulation model in a non-hydrostatic configuration
186 (MITgcm, Marshall et al. 1997). Here, we conduct new three-dimensional large-eddy simulations
187 of a line glacial meltwater plume rising next to a wall using the software package Oceananigans.jl
188 (Ramadhan et al. 2020). Oceananigans.jl is written in the high-level Julia programming language
189 (Bezanson et al. 2017), simulates the rotating non-hydrostatic incompressible Boussinesq equations
190 using a finite volume discretization similar to that of the MITgcm, and is optimized to run on
191 Graphical Processing Units (GPUs). The equations are integrated using a second-order Adams-
192 Bashforth scheme with adaptive time stepping. The effects of sub-grid scale processes are
193 parameterized via an eddy viscosity and eddy diffusivity modeled using the anisotropic minimum
194 dissipation (AMD) large-eddy simulation closure (Rozema et al. 2015). The AMD formalism was
195 refined by Verstappen (2018) and validated for ocean-relevant scenarios by Vreugdenhil and Taylor
196 (2018).

197 Our model domain follows the schematic in Figure 1. The horizontal widths L_y and L_x are
198 both set to 5 km, while the depth of the ice shelf front L_z is set equal to 400m (approximately
199 consistent with Pine Island Glacier, see Jenkins et al. 2010). The domain is re-entrant in the
200 zonal x -direction; free-slip and no-normal-flow conditions apply at the other boundaries. We use
201 512 grid cells in each horizontal direction and 96 grid cells in the vertical: this corresponds to a
202 horizontal resolution of 9.77 m and a vertical resolution of 4.17 m. We consider the evolution of
203 temperature, salinity, and a passive tracer representing meltwater. Glacial meltwater escaping from
204 underneath the ice shelf is represented as a constant buoyancy source F applied to a horizontal
205 area of length L next to the southern edge of the domain (see Figure 1). We conduct experiments
206 both with varying L and with L set to a default value of 1 km, which is broadly consistent with the
207 meltwater outflow from beneath Pine Island Glacier (Naveira Garabato et al. 2017). The buoyancy

208 source F is implemented as a constant volume-conserving “virtual salinity flux” (Huang 1993; see
209 Appendix B for details). The Coriolis parameter, f , is set to $-1.4 \times 10^{-4} \text{ s}^{-1}$, appropriate for the
210 latitude of Pine Island.

211 3. Results

212 a. *The simulated meltwater plume*

213 The basic behavior of the simulated glacial meltwater plume is demonstrated in Figure 3; here,
214 $F/L = 10^{-2} \text{ m}^3/\text{s}^3$. As in Figure 2, the initial condition is a uniform stratification of $N = 3 \times 10^{-3}$
215 s^{-1} ; this yields $N/f \approx 20$, similar to the meltwater plume simulations of Naveira Garabato et al.
216 (2017). For now, the stratification is implemented through a linear vertical salinity gradient, fixed
217 temperature, and a linear equation of state with haline contraction coefficient $\beta = 7.8 \times 10^{-4} \text{ psu}^{-1}$
218 (Vallis 2017). Here and throughout the paper we normalize plotted meltwater distributions to
219 integrate to 1. Following the evolution of the passive meltwater tracer, we see that the turbulent
220 plume initially rises rapidly, and then moves northward once it reaches neutral buoyancy. The
221 northward flow is deflected to the left by the Coriolis force, resulting in a strong westward jet;
222 this is consistent with the observations and two-dimensional simulations of Naveira Garabato et al.
223 (2017).

224 Next, we consider the time evolution of the horizontally averaged meltwater distribution over
225 one day of simulation. To quantify the effect that the Earth’s rotation may play in determining the
226 plume’s settling depth (e.g. Fabregat Tomàs et al. 2016; Naveira Garabato et al. 2017), we conduct
227 two simulations: one where the Coriolis parameter f has a realistic value $-1.4 \times 10^{-4} \text{ s}^{-1}$, and
228 one where f has been set to zero. The results of these experiments are shown in Figure 4. We
229 observe that, for this realistic choice of N/f , the meltwater’s settling depth is largely determined

230 on a timescale N^{-1} . As we approach a timescale of 1 day, the mean settling depths in the different
231 simulations diverge slightly: in the rotating case, the meltwater rises on average around 20m higher.
232 Additionally, the rotating experiment also shows a broadening of the vertical meltwater distribution
233 on this timescale, suggestive of rotational effects playing a mixing role.

234 Interestingly, these results conflict with those of Naveira Garabato et al. (2017), who used two-
235 dimensional simulations to argue that centrifugal instability is a dominant mechanism acting to
236 decrease the meltwater's rise height. As the northward-moving meltwater is deflected to the left
237 by the Coriolis force, a strong zonal jet develops (Figure 3); centrifugal instability can occur if the
238 resulting anticyclonic vorticity is large enough ($\zeta/f < -1$, Haine and Marshall 1998), promoting
239 lateral export and mixing of the meltwater. In their two-dimensional simulations, Naveira Garabato
240 et al. (2017), observed over the same timeframe of 1 day that setting $f = -1.4 \times 10^{-4} \text{ s}^{-1}$ was
241 sufficient to deepen the peak of the meltwater distribution by ~ 50 m compared to the case with $f =$
242 0, an effect that is absent in Figure 4. In Appendix C we address this discrepancy using additional
243 two-dimensional simulations: those results suggest that the effect observed in the simulations of
244 Naveira Garabato et al. (2017) may be related to their use of a restoring buoyancy source formulation
245 rather than a constant buoyancy source formulation as implemented in this study.

246 The effect of rotation on the meltwater settling depth in our simulations is smaller than that found
247 by Naveira Garabato et al. (2017), and has the opposite sign. This effect is relatively unimportant
248 compared to the role played by the buoyancy source per unit width (F/L) and ambient stratification
249 (N): this can be inferred both from Figure 2 and the rapid initial stratification-driven adjustment in
250 Figure 4, and is confirmed in the large-eddy simulations presented in the next section (Figure 5).
251 The effect emerges on the same timescale in which the meltwater flow reaches $x = 0$ after having
252 re-entered from the eastern boundary (~ 1 day, see Figure 3), and may thus also be a consequence
253 of the idealized nature of the simulation setup. For the purposes of this study, we remain agnostic

as to whether this effect represents a physical mechanism operating in the real world, and simply conclude the following. First, for realistic values of N/f , centrifugal instability is not important in determining the meltwater's settling depth. Second, rotational effects in general play at most a small role in determining the meltwater's settling depth, compared to the role played by F , L , and N .

b. Vertical meltwater distribution: uniform stratification

Now, we can evaluate how the meltwater's settling depth depends on the buoyancy source and the background stratification. We conduct a set of simulations where F , L and N are separately varied: the vertical meltwater distributions after 6 hours of integration are shown in Figure 5. We choose this timescale because by this point the depth of the meltwater has approximately stabilized (Figure 4). The default values of F , L and N in Figure 5 are $10 \text{ m}^4/\text{s}^3$, 1 km and $3 \times 10^{-3} \text{ s}^{-1}$. Because F is not necessarily an intuitively accessible quantity, for the case of varying F we included as an additional x-axis an approximate lower bound on the corresponding glacial mass loss due to melt (Appendix D). On top of the distributions obtained from the simulations we also plot predictions from the simple scaling solution and the one-dimensional line plume model presented above. Both show excellent agreement with the high-resolution simulations, suggesting that they parametrize the settling depth extremely well in these idealized conditions. For the scaling solution, we have used $a = 2.6$: the good agreement with the simulation results indicates that the coefficient matches that for point source plumes (Speer and Marshall 1995; Fabregat Tomàs et al. 2016).

c. Vertical meltwater distribution: non-uniform stratification

In the real world, the buoyancy frequency N is non-uniform in time and space. For example, observations from Pine Island Bay show that vertical profiles of temperature, salinity, and

276 meltwater fraction display significant interannual variability (Dutrieux et al. 2014b). In Figure
277 6 we demonstrate this variability by plotting temperature and salinity profiles collected next to
278 the meltwater outflow from Pine Island Glacier in 2009 and 2014 (Jacobs et al. 2011; Heywood
279 et al. 2016), together with estimates of the corresponding meltwater fractions. Notably, in 2009
280 meltwater was primarily centered at a depth of 400m, while in 2014 it was able to rise to the
281 surface. This difference appears too dramatic to be explained purely by interannual variability in
282 meltwater fluxes. For example, because of the $h \propto F^{1/3}$ scaling, changing rise height by even a
283 factor of 2 requires F to change by a factor of 8; meanwhile, observations indicate that meltwater
284 export from beneath the Pine Island ice shelf has varied by at most by a factor of 3 between years
285 (Dutrieux et al. 2014b). Hence, we propose that the variability in stratification played a major role.

286 We investigate the effect of the different background conditions in 2009 and 2014 by using
287 the top 400m of the observed temperature and salinity profiles as our initial conditions in our
288 high-resolution simulations. From these, Oceananigans.jl calculates a density profile using the
289 idealized nonlinear equation of state proposed by Roquet et al. (2015), optimized for near freezing.
290 We consider two different buoyancy sources, $F/L = 10^{-3} \text{ m}^3/\text{s}^3$ and $F/L = 10^{-2} \text{ m}^3/\text{s}^3$; these
291 values are chosen specifically to help illustrate the important dynamics. The vertical meltwater
292 distributions after 6 hours are shown in Figure 7. We additionally plot an estimate of the strength
293 of the initial stratification as a function of depth; this is obtained by calculating $N^2 = -\frac{g}{\rho_0} \frac{d\rho}{dz}$ for
294 each vertically adjacent pair of data points and applying a moving average with a 20m window to
295 identify important trends. For the case of $F/L = 10^{-2} \text{ m}^3/\text{s}^3$, we see that there is little difference in
296 the vertical meltwater distribution between 2009 and 2014 conditions. However, the simulations
297 with $F/L = 10^{-3} \text{ m}^3/\text{s}^3$ show a marked difference: in the 2009 case, meltwater settles at ~ 350 m
298 depth, while in the 2014 case it rises around 100m further. Finally, we have also plotted the settling
299 depths predicted by the one-dimensional plume model, using the same initial stratification profiles:

300 there is near-perfect agreement with the peaks of the meltwater distributions obtained from our
301 high-resolution simulations.

302 The behavior exhibited in the simulations with $F/L = 10^{-3} \text{ m}^3/\text{s}^3$ is qualitatively consistent
303 with the observations (Figure 6): namely, meltwater rose much higher in 2014. The lack of full
304 quantitative agreement is expected, because we have simulated only the top 400m of the water
305 column, neglected changes in the sub-ice-shelf meltwater dynamics, and neglected other real-
306 world processes that could affect the settling depth (such as changes in the ambient circulation
307 or wind-driven upwelling). We suggest that the difference in settling depths between our 2009
308 and 2014 simulations is a consequence of the N^2 peak at around 350 m that was present in
309 2009 but not in 2014: the meltwater was “trapped” by the local maximum in stratification. This
310 illustrates an important point: localized variability in the ambient stratification $N(z)$ can have
311 a substantial effect on meltwater settling depth even when the effective buoyancy flux remains
312 constant. When the buoyancy source is larger ($F/L = 10^{-2} \text{ m}^3/\text{s}^3$), the meltwater can “break
313 through” the stratification maximum, and ends up with a vertical distribution very similar to the
314 corresponding 2014 stratification profile.

315 4. Discussion

316 The potency of Antarctic glacial meltwater as a driver of regional and global climate trends
317 likely depends strongly on its settling depth or vertical distribution after exiting the ice shelf cavity.
318 Specifically, it seems feasible that meltwater could only explain the signs of the observed Southern
319 Ocean trends (surface cooling, surface freshening, and sea-ice expansion) as long as it rises close
320 enough to the surface to shoal the mixed layer base and to yield a measurable surface salinity
321 anomaly. Pauling et al. (2016), who considered the effects of releasing freshwater at different
322 depths, found that the depth of meltwater release had no significant effect on the magnitude of sea-

ice expansion. However, they also found a much weaker response of sea-ice expansion to freshwater forcing than other studies (Bintanja et al. 2013, 2015; Rye et al. 2020); these inter-model differences deserve further study. Observational data (e.g. Loose et al. 2009; Dutrieux et al. 2014b; Kim et al. 2016; Naveira Garabato et al. 2017; Biddle et al. 2019) highlight that meltwater can settle at a range of depths in the Subpolar Sea, suggesting that time-varying environmental conditions and the properties of individual meltwater plumes play important roles in determining the vertical distribution of meltwater in the Shelf Seas, and therefore the climate impact of meltwater anomaly production.

In Figure 8, we identify two different paradigms for introducing Antarctic meltwater fluxes into simulations of global climate. In paradigm A, meltwater fluxes (from observations or melt rate models) are inserted into the ocean model at some fixed vertical level. This paradigm has dominated the literature: as described earlier, most climate modeling studies have introduced all of the meltwater flux at the surface. In other studies, the meltwater has been uniformly distributed over a fixed range of depths below the ice shelf front (Beckmann and Goosse 2003; Mathiot et al. 2017). Given the likely climatic importance of Antarctic glacial meltwater, the strong dependence of settling depth on buoyancy release (e.g. as explored in this study), and the vast heterogeneity in the observed mass loss rates and ambient conditions at different ice shelves (Rignot et al. 2019), any such "one-size-fits-all" solution risks missing substantial aspects of the climate response to Antarctic mass loss. However, an alternative approach is possible: in paradigm B, the melt rate model is coupled to a dynamic plume model that describes the small-scale dynamics of buoyant meltwater plumes and accurately calculates the vertical distribution of meltwater. The meltwater is then inserted into the ocean model in accordance with this distribution.

Parametrizing the depth of meltwater input into general circulation models using buoyant plume theory is not a new idea: Cowton et al. (2015) have employed this technique to conduct more

347 efficient simulations of Arctic glacial fjords. Because Arctic tidewater glaciers are essentially
348 vertical for the entire depth of the water column, a single one-dimensional plume model can be
349 used to calculate both melt rates and plume dynamics. However, this is not true in the context of
350 Antarctic ice shelves, in part because of the large discontinuity in slope that occurs at the base of
351 the ice-shelf front. Therefore, a number of issues remain to be solved before paradigm B could be
352 implemented in simulations of global climate.

353 In this study we have shown that the settling depth of the meltwater after its escape from beneath
354 the ice shelf is well described by one-dimensional plume theory even for complex non-uniform
355 stratification (Figure 7), however, the critical input parameter F/L remains a function of complex
356 sub-ice-shelf processes. If the ‘melt rate model’ in Figure 8 is a box model (Olbers and Hellmer
357 2010; Reese et al. 2018), F could be estimated from the properties of the outflow from the box
358 closest to the ice-shelf front. If it is a plume model (MacAyeal 1985; Jenkins 2011; Lazeroms et al.
359 2018; Pelle et al. 2019), F could be estimated from the remaining buoyancy flux at the ice-shelf
360 front. However, both types of models may have issues calculating L , because they do not resolve
361 gyre circulations below the ice shelf (Grosfeld et al. 1997; Losch 2008; De Rydt et al. 2014), and
362 the focusing of meltwater outflows by kilometer-scale channels at the base of the ice (Dutrieux
363 et al. 2013, 2014a; Naveira Garabato et al. 2017).

364 Finally, one-dimensional plume models have fundamental limitations even in the relatively simple
365 case of a plume rising next to a vertical wall. For example, this neglects the along-shelf dynamics,
366 which affect the plume’s location and width as well the relevant ice shelf front depth, and have been
367 shown to significantly affect total melt rates in the Arctic context (Jackson et al. 2020). However, the
368 most significant limitation of using one-dimensional plume models to compute meltwater settling
369 depths is that these one-dimensional parameterizations can only output a single meltwater settling
370 depth ($B(z) = 0$). Meanwhile, observed vertical meltwater distributions can have complex, possibly

371 multi-modal shapes. Short of explicitly resolving the small-scale fluid dynamics of the meltwater
372 plume next to and below the entire ice shelf, it may be possible to extend upon the one-dimensional
373 plume model, perhaps by introducing a time dependence, to explicitly include a passive meltwater
374 tracer that would allow for the calculation of a vertical distribution rather than just its peak.

375 5. Conclusion

376 Antarctic glacial meltwater is likely an important driver of observed Southern Ocean climate
377 trends (Bintanja et al. 2013; Rye et al. 2014; Bintanja et al. 2015; Rye et al. 2020), and will have
378 a significant impact throughout the twenty-first century (Bronselaer et al. 2018; Golledge et al.
379 2019). Nevertheless, the factors determining the vertical distribution of meltwater in the water
380 column remain poorly understood. Here, we have used a hierarchy of approaches, spanning simple
381 scaling laws to high-resolution large-eddy simulations of the meltwater outflow from beneath an
382 ice shelf, to gain a fundamental understanding of the most important controls on the meltwater's
383 settling depth. We found that the settling depth is primarily a function of the buoyancy forcing per
384 unit width and the ambient stratification, consistent with the classical theory of turbulent buoyant
385 plumes and in contrast to previous suggestions that centrifugal instability plays an important role
386 (Naveira Garabato et al. 2017). Our simulations also provide insight into the observed interannual
387 variability in meltwater settling depth, using Pine Island Glacier as an example; the role of the
388 non-uniform background stratification is highlighted. We expect that the results of this study
389 are relevant to a wide range of Antarctic ice shelves, in part because the focusing of sub-ice-shelf
390 meltwater into a narrow outflow is a fundamental consequence of a generic sub-ice-shelf circulation
391 (Grosfeld et al. 1997; Losch 2008; De Rydt et al. 2014). The work presented in this study is a first
392 step towards a dynamic parameterization of Antarctic meltwater settling depth for simulations of
393 global climate. Because of the likely climatic importance of Antarctic glacial meltwater, the strong

394 dependence of mass loss rates on buoyancy forcing, and the vast heterogeneity in the observed
395 mass loss rates and ambient conditions at different ice shelves, such a parameterization could be
396 crucial for the accurate simulation and forecasting of high-latitude climate in a warming world.

397 *Acknowledgments.* We thank Alberto Naveira Garabato for discussions that helped motivate this
398 work, Gianluca Meneghelli and Jean-Michel Campin for discussions that aided in its execution, and
399 two reviewers for comments that greatly improved the manuscript. J. M. and C. D. R. acknowledge
400 support from the NASA MAP program and the MIT-GISS cooperative agreement. A. R. was
401 supported through the CliMA initiative funded by the Eric and Wendy Schmidt foundation. P. D.
402 was supported by NSF OPP award 1643285 and his Center for Climate and Life Fellowship from
403 the Earth Institute of Columbia University.

404 *Data availability statement.* This study generated no new data. Code for the one-dimensional
405 line plume model and the two- and three-dimensional large-eddy simulations is available at
406 <https://github.com/arnscheidt/antarctic-meltwater-settling-depth>.

407 APPENDIX A

408 **One-dimensional line plume model**

409 We construct a 1-dimensional vertical line plume model in the spirit of Morton et al. (1956). Here,
410 the rate of turbulent entrainment of ambient fluid into the rising buoyant plume is parametrized as
411 proportional to the plume's vertical velocity via an entrainment coefficient, α . We assume that the
412 vertical velocity w is uniform within the plume and zero outside, and that the plume is rising next
413 to a wall (so that entrainment can only occur from one side). We can then write down volume,
414 momentum, and mass conservation equations within the plume:

$$\frac{d}{dz}(Dw) = \alpha w \quad (\text{A1})$$

415

$$\frac{d}{dz}(Dw\rho_w) = Dg(\rho_a - \rho) \quad (\text{A2})$$

416

$$\frac{d}{dz}(Dw\rho) = \alpha w \rho_a. \quad (\text{A3})$$

417 Here, $\rho(z)$ is the density of the plume, $\rho_a(z)$ is the ambient density, D is the width of the plume
 418 perpendicular to the wall, and α is the entrainment coefficient. Assuming that $\rho(z)$ differs only
 419 slightly from the reference density ρ_0 , we can rewrite Equation (A2) as

$$\frac{d}{dz}(Dw^2) = D\frac{g}{\rho_0}(\rho_a - \rho). \quad (\text{A4})$$

420 Following the reasoning in Morton et al. (1956), we can use Equation (A1) to rewrite Equation
 421 (A3) as

$$\frac{d}{dz}(Dw\rho) = \rho_a \frac{d}{dz}(Dw) = \frac{d}{dz}(Dw\rho_a) - Dw \frac{d}{dz}\rho_a, \quad (\text{A5})$$

422 such that

$$\frac{d}{dz}(Dw(\rho_a - \rho)) = Dw \frac{d\rho_a}{dz}. \quad (\text{A6})$$

423 Now, writing $Dw = Q$ (volume flux), $Dw^2 = M$ (momentum flux) and $Dwg \frac{(\rho_a - \rho)}{\rho_0} = B$ (buoyancy
 424 flux), we obtain the three coupled ODEs

$$\frac{dQ}{dz} = \alpha \frac{M}{Q} \quad (\text{A7})$$

425

$$\frac{dM}{dz} = \frac{QB}{M} \quad (\text{A8})$$

426

$$\frac{dB}{dz} = Q \frac{g}{\rho_0} \frac{d\rho_a}{dz} = -QN^2. \quad (\text{A9})$$

427 These equations are similar but not equivalent to the corresponding equations for point plumes.
 428 Furthermore, each of the three governing equations has implicitly been divided by a factor of L
 429 (x-width of the plume); thus, all of the quantities Q, M, B are fluxes per unit width.

APPENDIX B

Buoyancy source implementation

432 We implement the buoyancy source F (m^4/s^3) in our high-resolution simulations as a volume-
 433 conserving “virtual salinity flux” (Huang 1993). The conservation law for an arbitrary tracer c in
 434 Oceananigans.jl is

$$\frac{\partial c}{\partial t} + \mathbf{u} \cdot \nabla c = -\nabla \cdot \mathbf{q}_c + F_c, \quad (\text{B1})$$

435 where \mathbf{q}_c is a diffusive flux and F_c is an external source term. In our simulations, we introduce
 436 the buoyancy uniformly across a volume that extends width L in the x -direction, 10 grid cells in
 437 the y -direction (~ 100 m), and one grid cell in the z -direction (~ 4 m). The width of 100m in the
 438 y -direction is chosen in part to simulate the fact that the plume has nonzero horizontal momentum
 439 when emerging from beneath the ice shelf, while still remaining consistent with observations and
 440 prior simulations of this scenario (Naveira Garabato et al. 2017). Including this initial velocity
 441 explicitly would impact the effect of the Coriolis force on the dynamics (e.g. strengthening the jet
 442 in Figure 3), but it is unclear to what extent this would affect the meltwater settling depth; we leave
 443 this as a question for future work. Defining the buoyancy source volume as V_b , we can write

$$\int_{V_b} dV \frac{db}{dt}_{\text{source}} = F, \quad (\text{B2})$$

444 where $\frac{db}{dt}_{\text{source}}$ refers only to the term within the full buoyancy conservation equation that comes
 445 from the external buoyancy source. Now, recall that

$$b = -\frac{g}{\rho_0}(\rho - \rho_0), \quad (\text{B3})$$

446 and that, to first order,

$$\rho = \rho_0(1 - \alpha(T - T_0) + \beta(S - S_0)). \quad (\text{B4})$$

⁴⁴⁷ Thus, if no temperature forcing is introduced,

$$\frac{db}{dt}_{\text{source}} = \frac{db}{d\rho} \frac{d\rho}{dt}_{\text{source}} = -\frac{g}{\rho_0} \frac{d\rho}{dt}_{\text{source}} = -g\beta \frac{dS}{dt}_{\text{source}}, \quad (\text{B5})$$

⁴⁴⁸ and, by (B2):

$$F = - \int_{V_b} dV g\beta \frac{dS}{dt}_{\text{source}} \equiv -g\beta F_S, \quad (\text{B6})$$

⁴⁴⁹ where F_S is the volume-integrated salinity flux ($\text{psu m}^3/\text{s}$). For a chosen F we therefore obtain a
⁴⁵⁰ corresponding F_S by (B6). Then, in our simulations, we distribute F_S uniformly across V_b .

⁴⁵¹ APPENDIX C

⁴⁵² **Restoring buoyancy sources may exaggerate the importance of rotational effects in** ⁴⁵³ **determining the meltwater's settling depth**

⁴⁵⁴ Our results conflict with those of Naveira Garabato et al. (2017). Using a two-dimensional
⁴⁵⁵ model, they found that including realistic rotation deepened the peak of the observed meltwater
⁴⁵⁶ distribution by ~ 50 m compared to a non-rotating case, after one day of integration. To clarify why
⁴⁵⁷ there is a discrepancy, we conduct additional two-dimensional simulations with Oceananigans.jl
⁴⁵⁸ that are designed to closely replicate those of Naveira Garabato et al. (2017).

⁴⁵⁹ The model domain spans $5\text{km} \times 300\text{m}$ and is zonally re-entrant. Our resolution is 512×96 , i.e.
⁴⁶⁰ $\sim 10\text{m} \times 3\text{m}$. The initial stable stratification is implemented using a linear equation of state and a
⁴⁶¹ linear temperature gradient from 1°C at the bottom to 3°C at the top. At the northern boundary,
⁴⁶² we continuously relax back to the stable initial condition. At the base of the southern boundary we
⁴⁶³ introduce meltwater via an unstable restoring region that extends 160m in the y-direction. In the
⁴⁶⁴ unstable restoring region, temperature is relaxed to a temperature $T_r(y)$, which is set following a
⁴⁶⁵ linear gradient: its value is 2°C at $y = 0$ m and 1°C at $y = 160$ m. For clarity, in the buoyancy

466 source region:

$$\frac{dT}{dt} = (\text{other terms}) + \lambda(T_r(y) - T), \quad (\text{C1})$$

467 where $\lambda = 1/20 \text{ s}^{-1}$. This experiment is conducted twice, once with $f = -1.4 \times 10^{-4} \text{ s}^{-1}$ (realistic
468 rotation) and once with $f = 0$ (no rotation). We then conduct an additional set of simulations using
469 a constant buoyancy source, which is set to approximately yield the same settling depth.

470 Figure 9 shows the vertical distribution of glacial melt in the water column after 1 day, for
471 both rotating and non-rotating cases, and for a restoring formulation and a constant buoyancy
472 source formulation. When a restoring formulation is used, in the rotating case the peak is $\sim 50 \text{ m}$
473 deeper than in the non-rotating case, consistent with the results of Naveira Garabato et al. (2017).
474 However, when a constant buoyancy source is used, rotation appears to have no effect on the peak
475 of the meltwater distribution. Since the magnitude of the buoyancy source is a primary control
476 on the meltwater's settling depth, the importance of any other parameters can only be accurately
477 investigated by holding the buoyancy source constant. This suggests that the bottom results in
478 Figure 9 are more physical, and that the use of restoring non-constant buoyancy sources may
479 exaggerate the effect of rotation on the settling depth.

480 APPENDIX D

481 Approximate lower bound on net melting corresponding to a given buoyancy source

482 For the second x -axis included in Figure 5 (A), we estimate a lower bound on the glacial mass
483 loss due to melt (i.e. net melting) corresponding to a buoyancy source F (m^4/s^3). In the real
484 world, melting is spatially distributed throughout the ice-shelf cavity, and the meltwater that is
485 released loses buoyancy as it ascends towards the ice-shelf front. If the meltwater plume carries a
486 buoyancy flux F by the time it reaches the base of the ice shelf (i.e. the base of our model domain),

⁴⁸⁷ the smallest possible rate of mass loss that could be responsible for that buoyancy flux would be
⁴⁸⁸ achieved if all the melting had occurred at precisely that depth.

⁴⁸⁹ To obtain a lower bound on the mass loss corresponding to a given F , therefore, let us assume
⁴⁹⁰ that F arises entirely from melting occurring at the base of our model domain (i.e. the base of the
⁴⁹¹ ice-shelf front). If this represents pure freshwater, the buoyancy gained by its input into the system
⁴⁹² is equivalent to the buoyancy gained by removing the same volume of water at the ambient salinity
⁴⁹³ S_0 (set to 34.6 psu). This can be justified rigorously by noting that, if we add a small volume of
⁴⁹⁴ water ΔV with salinity 0 to a large volume of water V with salinity S_0 , the new salinity is given by

$$S_0 + \Delta S = \frac{VS_0}{V + \Delta V} \simeq S_0 \left(1 - \frac{\Delta V}{V}\right) \quad (\text{D1})$$

⁴⁹⁵ i.e.

$$V\Delta S \simeq -S_0\Delta V. \quad (\text{D2})$$

⁴⁹⁶ Moving from volumes to fluxes, let F_M denote our lower bound on the mass flux (kg/s). Following
⁴⁹⁷ (D2), the volume-integrated virtual salinity flux F_S (psu m³/s) is given by

$$F_S \simeq -S_0 \frac{F_M}{\rho_0}. \quad (\text{D3})$$

⁴⁹⁸ Using (B6), we find that

$$F_M \simeq \frac{\rho_0 F}{g\beta S_0}, \quad (\text{D4})$$

⁴⁹⁹ where F is the buoyancy flux (m⁴/s³).

⁵⁰⁰ A complementary interpretation of F_M is the following: for a mass loss flux of F_M , the meltwater
⁵⁰¹ may rise no higher than the settling depth shown in Figure 5.

⁵⁰² References

⁵⁰³ Beckmann, A., and H. Goosse, 2003: A parameterization of ice shelf–ocean interaction for climate
⁵⁰⁴ models. *Ocean modelling*, **5** (2), 157–170, doi:10.1016/S1463-5003(02)00019-7.

- 505 Bezanson, J., A. Edelman, S. Karpinski, and V. B. Shah, 2017: Julia: A fresh approach to numerical
506 computing. *SIAM review*, **59** (1), 65–98, doi:10.1137/141000671.
- 507 Biddle, L. C., B. Loose, and K. J. Heywood, 2019: Upper ocean distribution of glacial meltwater in
508 the Amundsen Sea, Antarctica. *Journal of Geophysical Research: Oceans*, **124** (10), 6854–6870,
509 doi:10.1029/2019JC015133.
- 510 Bintanja, R., G. Van Oldenborgh, S. Drijfhout, B. Wouters, and C. Katsman, 2013: Important
511 role for ocean warming and increased ice-shelf melt in Antarctic sea-ice expansion. *Nature
512 Geoscience*, **6** (5), 376, doi:10.1038/ngeo1767.
- 513 Bintanja, R., G. Van Oldenborgh, and C. Katsman, 2015: The effect of increased fresh water
514 from Antarctic ice shelves on future trends in Antarctic sea ice. *Annals of Glaciology*, **56** (69),
515 120–126, doi:10.3189/2015AoG69A001.
- 516 Bronselaer, B., M. Winton, S. M. Griffies, W. J. Hurlin, K. B. Rodgers, O. V. Sergienko, R. J.
517 Stouffer, and J. L. Russell, 2018: Change in future climate due to Antarctic meltwater. *Nature*,
518 **564** (7734), 53, doi:10.1038/s41586-018-0712-z.
- 519 Carroll, D., D. A. Sutherland, E. L. Shroyer, J. D. Nash, G. A. Catania, and L. A.
520 Stearns, 2015: Modeling turbulent subglacial meltwater plumes: Implications for fjord-scale
521 buoyancy-driven circulation. *Journal of Physical Oceanography*, **45** (8), 2169–2185, doi:
522 10.1175/JPO-D-15-0033.1.
- 523 Cowton, T., D. Slater, A. Sole, D. Goldberg, and P. Nienow, 2015: Modeling the impact of glacial
524 runoff on fjord circulation and submarine melt rate using a new subgrid-scale parameterization
525 for glacial plumes. *Journal of Geophysical Research: Oceans*, **120** (2), 796–812, doi:10.1002/
526 2014JC010324.

- 527 De Rydt, J., P. Holland, P. Dutrieux, and A. Jenkins, 2014: Geometric and oceanographic controls
528 on melting beneath Pine Island Glacier. *Journal of Geophysical Research: Oceans*, **119** (4),
529 2420–2438, doi:10.1002/2013JC009513.
- 530 Dutrieux, P., C. Stewart, A. Jenkins, K. W. Nicholls, H. F. Corr, E. Rignot, and K. Steffen, 2014a:
531 Basal terraces on melting ice shelves. *Geophysical Research Letters*, **41** (15), 5506–5513, doi:
532 10.1002/2014GL060618.
- 533 Dutrieux, P., D. G. Vaughan, H. F. Corr, A. Jenkins, P. R. Holland, I. Joughin, and A. Fleming,
534 2013: Pine Island glacier ice shelf melt distributed at kilometre scales. *The Cryosphere*, **7** (5),
535 1543–1555, doi:10.5194/tc-7-1543-2013.
- 536 Dutrieux, P., and Coauthors, 2014b: Strong sensitivity of Pine Island ice-shelf melting to climatic
537 variability. *Science*, **343** (6167), 174–178, doi:10.1126/science.1244341.
- 538 Ezhova, E., C. Cenedese, and L. Brandt, 2018: Dynamics of three-dimensional turbulent wall
539 plumes and implications for estimates of submarine glacier melting. *Journal of Physical*
540 *Oceanography*, **48** (9), 1941–1950, doi:10.1175/JPO-D-17-0194.1.
- 541 Fabregat Tomàs, A., A. C. Poje, T. M. Özgökmen, and W. K. Dewar, 2016: Effects of rotation on
542 turbulent buoyant plumes in stratified environments. *Journal of Geophysical Research: Oceans*,
543 **121** (8), 5397–5417, doi:10.1002/2016JC011737.
- 544 Golledge, N. R., E. D. Keller, N. Gomez, K. A. Naughten, J. Bernales, L. D. Trusel, and T. L.
545 Edwards, 2019: Global environmental consequences of twenty-first-century ice-sheet melt.
546 *Nature*, **566** (7742), 65–72, doi:10.1038/s41586-019-0889-9.

- 547 Gourmelen, N., and Coauthors, 2017: Channelized melting drives thinning under a rapidly
548 melting Antarctic ice shelf. *Geophysical Research Letters*, **44** (19), 9796–9804, doi:10.1002/
549 2017GL074929.
- 550 Grosfeld, K., R. Gerdes, and J. Determann, 1997: Thermohaline circulation and interaction
551 between ice shelf cavities and the adjacent open ocean. *Journal of Geophysical Research: Oceans*, **102** (C7), 15 595–15 610, doi:10.1029/97JC00891.
- 553 Haine, T. W., and J. Marshall, 1998: Gravitational, symmetric, and baroclinic instability of
554 the ocean mixed layer. *Journal of physical oceanography*, **28** (4), 634–658, doi:10.1175/1520-0485(1998)028<0634:GSABIO>2.0.CO;2.
- 556 Hansen, J., and Coauthors, 2016: Ice melt, sea level rise and superstorms: evidence from
557 paleoclimate data, climate modeling, and modern observations that 2 C global warming
558 is highly dangerous. *Atmospheric Chemistry & Physics Discussions*, **16** (6), doi:10.5194/acp-16-3761-2016.
- 560 Helfrich, K. R., and T. M. Battisti, 1991: Experiments on baroclinic vortex shedding from
561 hydrothermal plumes. *Journal of Geophysical Research: Oceans*, **96** (C7), 12 511–12 518,
562 doi:10.1029/90JC02643.
- 563 Heywood, K. J., and Coauthors, 2016: Between the devil and the deep blue sea: the role of the
564 Amundsen Sea continental shelf in exchanges between ocean and ice shelves. *Oceanography*,
565 **29** (4), 118–129, doi:10.5670/oceanog.2016.104.
- 566 Holland, P. R., D. L. Feltham, and A. Jenkins, 2007: Ice shelf water plume flow beneath Filchner-
567 Ronne Ice Shelf, Antarctica. *Journal of Geophysical Research: Oceans*, **112** (C5), doi:10.1029/
568 2006JC003915.

- 569 Huang, R. X., 1993: Real freshwater flux as a natural boundary condition for the salinity balance
570 and thermohaline circulation forced by evaporation and precipitation. *Journal of Physical*
571 *Oceanography*, **23** (11), 2428–2446, doi:10.1175/1520-0485(1993)023<2428:RFFAAN>2.0.
572 CO;2.
- 573 Jackson, R., and Coauthors, 2020: Meltwater intrusions reveal mechanisms for rapid submarine
574 melt at a tidewater glacier. *Geophysical Research Letters*, **47** (2), e2019GL085 335, doi:10.1029/
575 2019GL085335.
- 576 Jacobs, S. S., A. Jenkins, C. F. Giulivi, and P. Dutrieux, 2011: Stronger ocean circulation and
577 increased melting under Pine Island Glacier ice shelf. *Nature Geoscience*, **4** (8), 519–523,
578 doi:10.1038/ngeo1188.
- 579 Jenkins, A., 1991: A one-dimensional model of ice shelf-ocean interaction. *Journal of Geophysical*
580 *Research: Oceans*, **96** (C11), 20 671–20 677, doi:10.1029/91JC01842.
- 581 Jenkins, A., 2011: Convection-driven melting near the grounding lines of ice shelves and tidewater
582 glaciers. *Journal of Physical Oceanography*, **41** (12), 2279–2294, doi:10.1175/JPO-D-11-03.1.
- 583 Jenkins, A., P. Dutrieux, S. S. Jacobs, S. D. McPhail, J. R. Perrett, A. T. Webb, and D. White,
584 2010: Observations beneath Pine Island Glacier in West Antarctica and implications for its
585 retreat. *Nature Geoscience*, **3** (7), 468, doi:10.1038/ngeo890.
- 586 Jiang, H., and J. A. Breier, 2014: Physical controls on mixing and transport within rising submarine
587 hydrothermal plumes: A numerical simulation study. *Deep Sea Research Part I: Oceanographic*
588 *Research Papers*, **92**, 41–55, doi:10.1016/j.dsr.2014.06.006.
- 589 Jones, J. M., and Coauthors, 2016: Assessing recent trends in high-latitude Southern Hemisphere
590 surface climate. *Nature Climate Change*, **6** (10), 917–926, doi:10.1038/nclimate3103.

- 591 Kim, I., D. Hahm, T. S. Rhee, T. W. Kim, C.-S. Kim, and S. Lee, 2016: The distribution of glacial
592 meltwater in the Amundsen Sea, Antarctica, revealed by dissolved helium and neon. *Journal of*
593 *Geophysical Research: Oceans*, **121** (3), 1654–1666, doi:10.1002/2015JC011211.
- 594 Kimura, S., P. R. Holland, A. Jenkins, and M. Piggott, 2014: The effect of meltwater plumes on
595 the melting of a vertical glacier face. *Journal of Physical Oceanography*, **44** (12), 3099–3117,
596 doi:10.1175/JPO-D-13-0219.1.
- 597 Kostov, Y., D. Ferreira, K. C. Armour, and J. Marshall, 2018: Contributions of greenhouse gas
598 forcing and the southern annular mode to historical southern ocean surface temperature trends.
599 *Geophysical Research Letters*, **45** (2), 1086–1097, doi:10.1002/2017GL074964.
- 600 Lavelle, J., 1995: The initial rise of a hydrothermal plume from a line segment source—Results
601 from a three-dimensional numerical model. *Geophysical research letters*, **22** (2), 159–162,
602 doi:10.1029/94GL01463.
- 603 Lazeroms, W., A. Jenkins, H. Gudmundsson, and R. van de Wal, 2018: Modelling present-day
604 basal melt rates for Antarctic ice shelves using a parametrization of buoyant meltwater plumes.
605 *The Cryosphere*, **12** (1), 49–70, doi:10.5194/tc-12-49-2018.
- 606 Loose, B., P. Schlosser, W. Smethie, and S. Jacobs, 2009: An optimized estimate of glacial melt
607 from the Ross Ice Shelf using noble gases, stable isotopes, and CFC transient tracers. *Journal*
608 *of Geophysical Research: Oceans*, **114** (C8), doi:10.1029/2008JC005048.
- 609 Losch, M., 2008: Modeling ice shelf cavities in a z-coordinate ocean general circulation model.
610 *Journal of Geophysical Research: Oceans*, **113** (C8), doi:10.1029/2007JC004368.
- 611 MacAyeal, D. R., 1985: Evolution of tidally triggered meltwater plumes below ice shelves.
612 *Oceanology of the Antarctic continental shelf*, **43**, 133–143, doi:10.1029/AR043p0133.

- 613 Marshall, J., A. Adcroft, C. Hill, L. Perelman, and C. Heisey, 1997: A finite-volume, incompressible
614 Navier Stokes model for studies of the ocean on parallel computers. *Journal of Geophysical*
615 *Research: Oceans*, **102 (C3)**, 5753–5766, doi:10.1029/96JC02775.
- 616 Mathiot, P., A. Jenkins, C. Harris, and G. Madec, 2017: Explicit and parametrised representation
617 of under ice shelf seas in the z* coordinate ocean model NEMO 3.6. *Geoscientific Model*
618 *Development*, **10 (7)**, 2849–2874, doi:10.5194/gmd-10-2849-2017.
- 619 Morton, B., G. I. Taylor, and J. S. Turner, 1956: Turbulent gravitational convection from maintained
620 and instantaneous sources. *Proceedings of the Royal Society of London. Series A. Mathematical*
621 *and Physical Sciences*, **234 (1196)**, 1–23, doi:10.1098/rspa.1956.0011.
- 622 Naveira Garabato, A. C., and Coauthors, 2017: Vigorous lateral export of the meltwater outflow
623 from beneath an Antarctic ice shelf. *Nature*, **542 (7640)**, 219, doi:10.1038/nature20825.
- 624 Olbers, D., and H. Hellmer, 2010: A box model of circulation and melting in ice shelf caverns.
625 *Ocean Dynamics*, **60 (1)**, 141–153, doi:10.1007/s10236-009-0252-z.
- 626 Paolo, F. S., H. A. Fricker, and L. Padman, 2015: Volume loss from Antarctic ice shelves is
627 accelerating. *Science*, **348 (6232)**, 327–331, doi:10.1126/science.aaa0940.
- 628 Pauling, A. G., C. M. Bitz, I. J. Smith, and P. J. Langhorne, 2016: The response of the Southern
629 Ocean and Antarctic sea ice to freshwater from ice shelves in an Earth system model. *Journal*
630 *of Climate*, **29 (5)**, 1655–1672, doi:10.1175/JCLI-D-15-0501.1.
- 631 Pelle, T., M. Morlighem, and J. H. Bondzio, 2019: Brief communication: PICOP, a new ocean
632 melt parameterization under ice shelves combining PICO and a plume model. *The Cryosphere*,
633 **13 (3)**, 1043–1049, doi:10.5194/tc-13-1043-2019.

- 634 Prince, P. J., and J. R. Dormand, 1981: High order embedded Runge-Kutta formulae. *Journal of*
635 *Computational and Applied Mathematics*, **7** (1), 67–75, doi:10.1016/0771-050X(81)90010-3.
- 636 Ramadhan, A., and Coauthors, 2020: Oceananigans.jl: Fast and friendly geophysical fluid
637 dynamics on GPUs. *Journal of Open Source Software*, **5** (53), 2018, doi:10.21105/joss.02018.
- 638 Reese, R., T. Albrecht, M. Mengel, X. Asay-Davis, and R. Winkelmann, 2018: Antarctic sub-shelf
639 melt rates via PICO. doi:10.5194/tc-12-1969-2018.
- 640 Rignot, E., J. Mouginot, B. Scheuchl, M. van den Broeke, M. J. van Wessem, and M. Morlighem,
641 2019: Four decades of Antarctic Ice Sheet mass balance from 1979–2017. *Proceedings of the*
642 *National Academy of Sciences*, **116** (4), 1095–1103, doi:10.1073/pnas.1812883116.
- 643 Roquet, F., G. Madec, L. Brodeau, and J. Nycander, 2015: Defining a simplified yet “realistic”
644 equation of state for seawater. *Journal of Physical Oceanography*, **45** (10), 2564–2579, doi:
645 10.1175/JPO-D-15-0080.1.
- 646 Rozema, W., H. J. Bae, P. Moin, and R. Verstappen, 2015: Minimum-dissipation models for
647 large-eddy simulation. *Physics of Fluids*, **27** (8), 085 107, doi:10.1063/1.4928700.
- 648 Rye, C. D., A. C. N. Garabato, P. R. Holland, M. P. Meredith, A. G. Nurser, C. W. Hughes, A. C.
649 Coward, and D. J. Webb, 2014: Rapid sea-level rise along the Antarctic margins in response to
650 increased glacial discharge. *Nature Geoscience*, **7** (10), 732, doi:10.1038/ngeo2230.
- 651 Rye, C. D., J. Marshall, M. Kelley, G. Russell, L. S. Nazarenko, Y. Kostov, G. A. Schmidt, and
652 J. Hansen, 2020: Antarctic Glacial Melt as a Driver of Recent Southern Ocean Climate Trends.
653 *Geophysical Research Letters*, doi:10.1029/2019GL086892.

- 654 Sciascia, R., F. Straneo, C. Cenedese, and P. Heimbach, 2013: Seasonal variability of submarine
655 melt rate and circulation in an East Greenland fjord. *Journal of Geophysical Research: Oceans*,
656 **118** (5), 2492–2506, doi:10.1002/jgrc.20142.
- 657 Shean, D. E., I. R. Joughin, P. Dutrieux, B. E. Smith, and E. Berthier, 2019: Ice shelf basal
658 melt rates from a high-resolution digital elevation model (DEM) record for Pine Island Glacier,
659 Antarctica. *The Cryosphere*, **13** (10), 2633–2656, doi:10.5194/tc-13-2633-2019.
- 660 Slater, D., P. Nienow, T. Cowton, D. Goldberg, and A. Sole, 2015: Effect of near terminus
661 subglacial hydrology on tidewater glacier submarine melt rates. *Geophysical Research Letters*,
662 **42** (8), 2861–2868, doi:10.1002/2014GL062494.
- 663 Slater, D. A., D. N. Goldberg, P. W. Nienow, and T. R. Cowton, 2016: Scalings for submarine
664 melting at tidewater glaciers from buoyant plume theory. *Journal of Physical Oceanography*,
665 **46** (6), 1839–1855, doi:10.1175/JPO-D-15-0132.1.
- 666 Speer, K. G., and J. Marshall, 1995: The growth of convective plumes at seafloor hot springs.
667 *Journal of marine research*, **53** (6), 1025–1057, doi:10.1357/0022240953212972.
- 668 Straneo, F., G. S. Hamilton, D. A. Sutherland, L. A. Stearns, F. Davidson, M. O. Hammill, G. B.
669 Stenson, and A. Rosing-Asvid, 2010: Rapid circulation of warm subtropical waters in a major
670 glacial fjord in East Greenland. *Nature Geoscience*, **3** (3), 182–186, doi:10.1038/ngeo764.
- 671 Swart, N., and J. Fyfe, 2013: The influence of recent Antarctic ice sheet retreat on simulated sea
672 ice area trends. *Geophysical Research Letters*, **40** (16), 4328–4332, doi:10.1002/grl.50820.
- 673 Taylor, K. E., R. J. Stouffer, and G. A. Meehl, 2012: An overview of CMIP5 and the
674 experiment design. *Bulletin of the American Meteorological Society*, **93** (4), 485–498, doi:
675 10.1175/BAMS-D-11-00094.1.

676 Thurnherr, A. M., S. Jacobs, P. Dutrieux, and C. Giulivi, 2014: Export and circulation of ice cavity
677 water in Pine Island Bay, West Antarctica. *Journal of Geophysical Research: Oceans*, **119** (3),
678 1754–1764, doi:10.1002/2013JC009307.

681 Timmermann, R., and Coauthors, 2010: A consistent data set of Antarctic ice sheet topography,
682 cavity geometry, and global bathymetry. *Earth System Science Data*, **2** (2), 261–273, doi:
683 10.5194/essd-2-261-2010.

684 Turner, J., 1986: Turbulent entrainment: the development of the entrainment assumption, and
685 its application to geophysical flows. *Journal of Fluid Mechanics*, **173**, 431–471, doi:10.1017/
686 S0022112086001222.

687 Turner, J., T. J. Bracegirdle, T. Phillips, G. J. Marshall, and J. S. Hosking, 2013: An initial
688 assessment of Antarctic sea ice extent in the CMIP5 models. *Journal of Climate*, **26** (5), 1473–
689 1484, doi:10.1175/JCLI-D-12-00068.1.

690 Vallis, G. K., 2017: *Atmospheric and oceanic fluid dynamics*. Cambridge University Press, doi:
691 10.1017/9781107588417.

692 Verstappen, R., 2018: How much eddy dissipation is needed to counterbalance the nonlinear
693 production of small, unresolved scales in a large-eddy simulation of turbulence? *Computers &*
694 Fluids, **176**, 276–284, doi:10.1016/j.compfluid.2016.12.016.

695 Vreugdenhil, C. A., and J. R. Taylor, 2018: Large-eddy simulations of stratified plane Couette
flow using the anisotropic minimum-dissipation model. *Physics of Fluids*, **30** (8), 085104,
doi:10.1063/1.5037039.

- 696 Xu, Y., E. Rignot, I. Fenty, D. Menemenlis, and M. M. Flexas, 2013: Subaqueous melting of Store
697 Glacier, west Greenland from three-dimensional, high-resolution numerical modeling and ocean
698 observations. *Geophysical Research Letters*, **40** (17), 4648–4653, doi:10.1002/grl.50825.
- 699 Xu, Y., E. Rignot, D. Menemenlis, and M. Koppes, 2012: Numerical experiments on subaqueous
700 melting of Greenland tidewater glaciers in response to ocean warming and enhanced subglacial
701 discharge. *Annals of Glaciology*, **53** (60), 229–234, doi:doi:10.3189/2012AoG60A139.

702 LIST OF FIGURES

- Fig. 1.** A schematic describing the object of study. Melt rate data (gold/red) are from Shean et al. (2019) and Gourmelen et al. (2017), and bathymetry data (blue/green) are from Timmermann et al. (2010). Light, medium, and dark gray represent ice shelves, the Antarctic ice sheet, and rock outcrops, respectively. We focus on the meltwater outflow from beneath Pine Island Glacier, which is concentrated in a narrow km-scale outflow at its western edge; this may be a feature of many Antarctic ice shelves. We idealize this meltwater outflow as a constant buoyancy source F , with width L , applied to the bottom of our model domain.

Fig. 2. Example solutions of the one-dimensional line plume model for different buoyancy forcings F/L . $h = 0$ represents the base of the ice shelf front. In each case, the black dot highlights the meltwater's settling depth; this is the level of neutral buoyancy, i.e. where $B(z) = 0$

Fig. 3. Evolution of a simulated meltwater plume, after 6 hours and after 18 hours. Row A depicts a yz -plane with $x = 0$ (i.e. perpendicular to the ice shelf front): arrows indicate the flow in this plane, while colors indicate the flow perpendicular to it. We see the development of a strong zonal flow, consistent with observations of the outflow from beneath the Pine Island ice shelf. Row B depicts the zonally averaged meltwater distribution, and row C depicts the meridionally averaged meltwater distribution. Distributions have been normalized to integrate to 1. The meltwater outflow is deflected to the west by the Coriolis force, and eventually re-enters the domain at the eastern boundary.

Fig. 4. The evolution of the horizontally averaged vertical meltwater distribution over 1 day of simulation, for a realistic value of the Coriolis parameter f and for a case where $f = 0$. A and B show the evolution of the distributions, and C shows the evolution of the mean settling depth. Here, $F = 10 \text{ m}^4/\text{s}^3$, and $L = 1 \text{ km}$. In our simulations, rotational effects broaden the distribution of meltwater over a wider range of depths. The effect on the mean settling depth is smaller and of the opposite sign as that found by Naveira Garabato et al. (2017); we discuss this in the text.

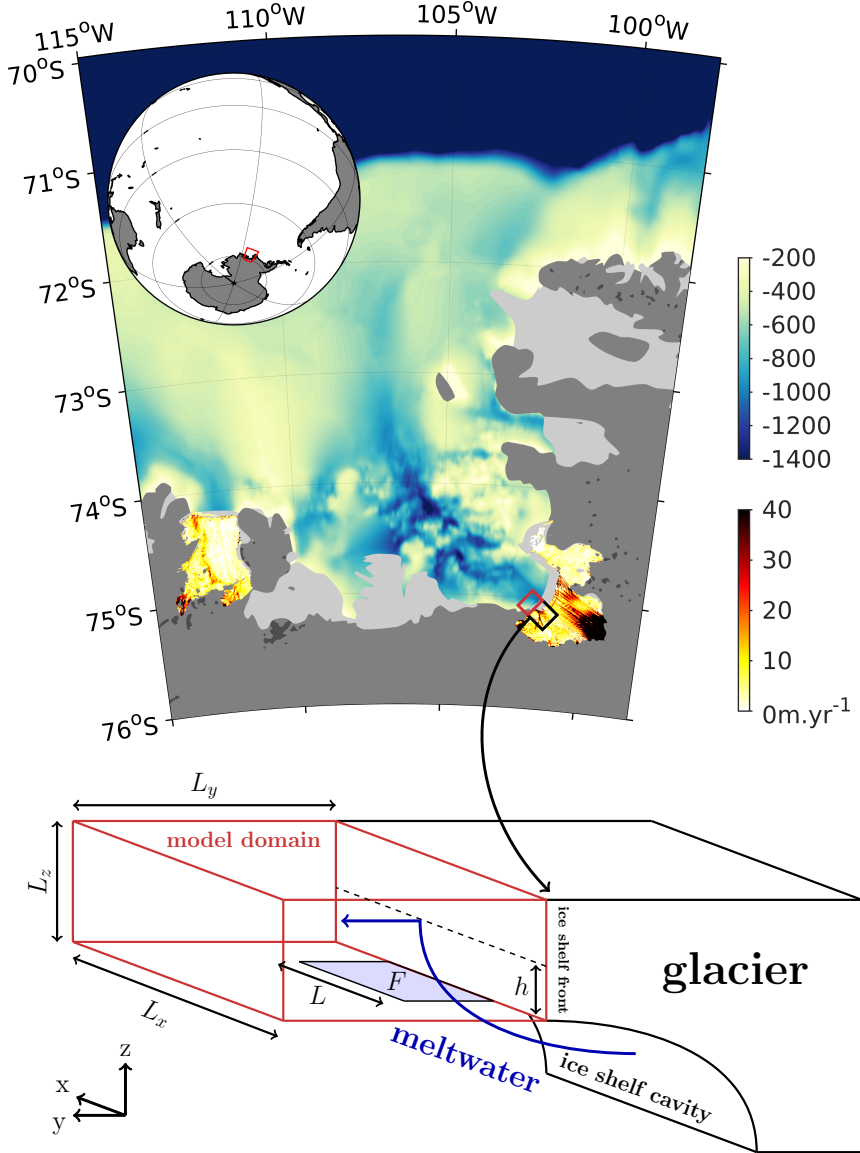
Fig. 5. The horizontally averaged vertical meltwater distribution after 6 hours of simulation, for varying buoyancy source F , varying stratification N , and varying outflow width L . For the case of varying F , we have also estimated a lower bound on the corresponding mass loss due to melt (see text). On top of the distributions we plot the settling depths predicted by the simple scaling relationships (dashed) and the one-dimensional line plume model (solid) with $a = 2.6$: both show excellent agreement with the high-resolution simulations. The new scaling relationships show substantial improvement over the scaling relationships for point source plumes ($h \propto (F/N^3)^{1/4}$).

Fig. 6. Observed 2009 and 2014 temperature and salinity profiles next to the meltwater outflow from Pine Island Glacier, as well as estimated meltwater fractions. In 2009, meltwater was primarily centered at a 400m depth, while in 2014 it was able to rise to the surface.

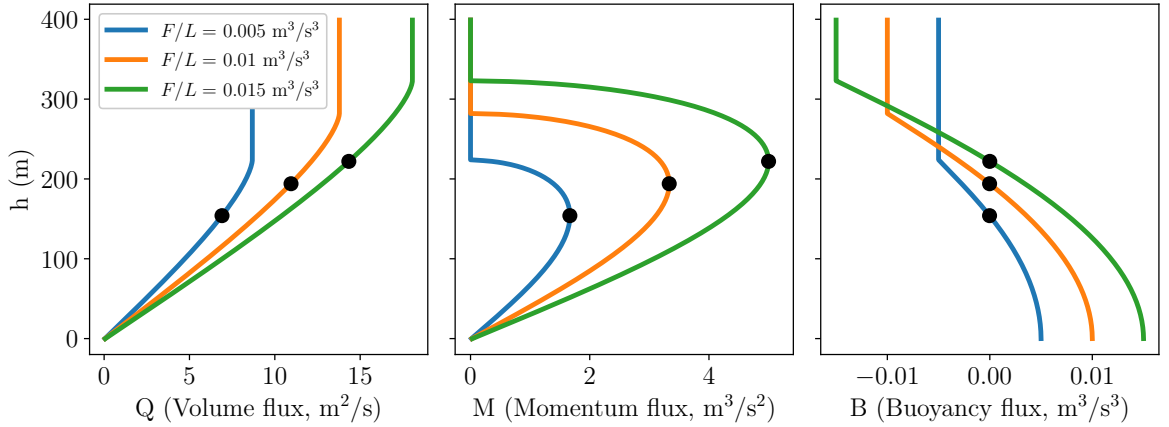
Fig. 7. Simulated vertical meltwater distributions (from LES, solid) for $F/L = 10^{-3} \text{ m}^3/\text{s}^3$ and $F/L = 10^{-2} \text{ m}^3/\text{s}^3$, with initial conditions set by observed temperature and salinity profiles for 2009 and 2014. Horizontal dashed lines indicate the settling depths predicted by the one-dimensional line plume model for the same conditions; notably, the line plume model accurately predicts the peak of the simulated meltwater distribution in all cases. We also plot depth profiles of stratification strength in terms of N^2 (see text). For $F/L = 10^{-2} \text{ m}^3/\text{s}^3$ we see that there is little difference in the vertical meltwater distribution between 2009 and 2014 conditions. However, the simulations with $F/L = 10^{-3} \text{ m}^3/\text{s}^3$ show a marked difference: the qualitative trend is consistent with observations (Figure 6). Here, we propose that the rising

Fig. 8. Schematic describing two different paradigms for Antarctic meltwater fluxes in simulations of global climate. In paradigm A, the fluxes from a melt rate model are inserted into the ocean model at some fixed vertical level; this approach has dominated the literature. In paradigm B, the melt rate model is coupled to a dynamic plume model that describes the small-scale dynamics of buoyant meltwater plumes and accurately calculates the vertical distribution of meltwater for insertion into the ocean model. Given the potential climatic importance of glacial meltwater, the strong dependence of settling depth on the buoyancy forcing, and the vast heterogeneity in the observed mass loss rates and ambient conditions at different ice shelves, this approach would likely represent a significant improvement over the “one-size-fits-all” approach of paradigm A.

Fig. 9. Vertical meltwater distributions, for rotating and non-rotating cases, in a two-dimensional domain. In panel A, we have introduced meltwater via a restoring buoyancy source (following Naveira Garabato et al. (2017), see text), while in panel B we have used a constant buoyancy source (as in the simulations described in the main text). When a constant buoyancy source is employed, the peak of the vertical distribution is not noticeably influenced by the effects of rotation. However, when a restoring buoyancy source is employed, rotation deepens the peak by ~ 50 m, consistent with the simulations of Naveira Garabato et al. (2017). Since the magnitude of the buoyancy source is a primary control on the meltwater's settling depth, the importance of any other parameters can only be accurately investigated by holding the buoyancy source constant; therefore, these results show that the use of restoring non-constant buoyancy sources may exaggerate the effect of rotation on the settling depth.



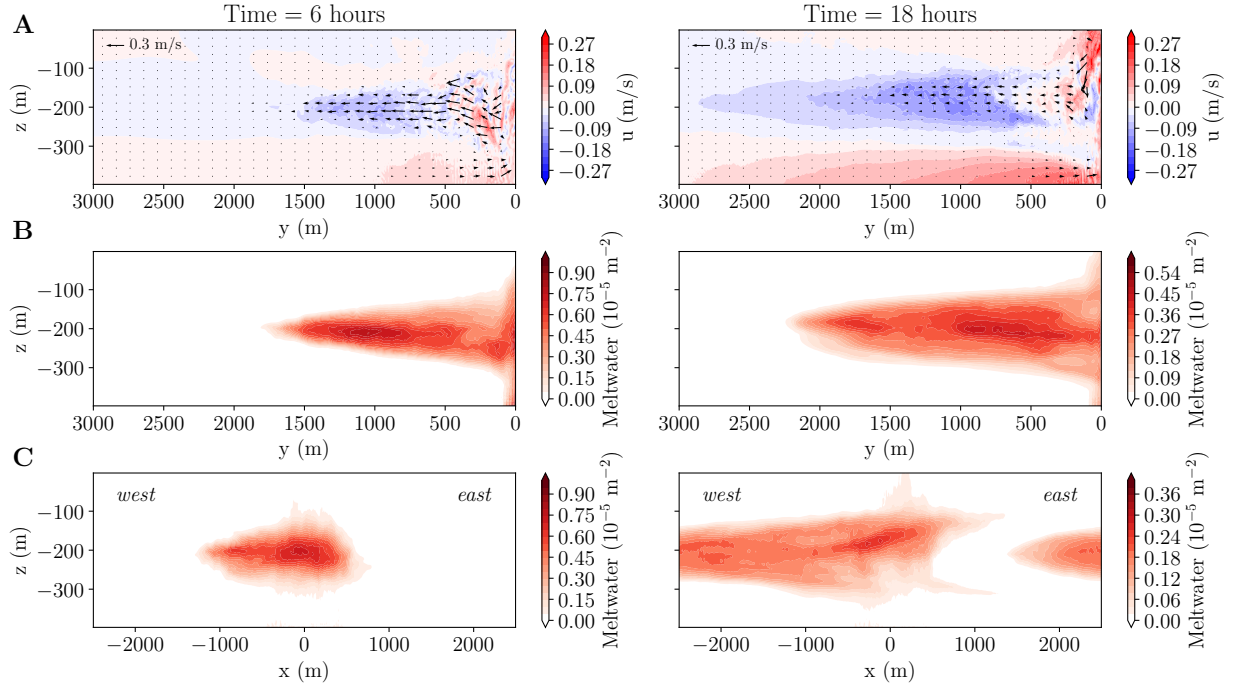
771 FIG. 1. A schematic describing the object of study. Melt rate data (gold/red) are from Shean et al. (2019) and
 772 Gourmelen et al. (2017), and bathymetry data (blue/green) are from Timmermann et al. (2010). Light, medium,
 773 and dark gray represent ice shelves, the Antarctic ice sheet, and rock outcrops, respectively. We focus on the
 774 meltwater outflow from beneath Pine Island Glacier, which is concentrated in a narrow km-scale outflow at its
 775 western edge; this may be a feature of many Antarctic ice shelves. We idealize this meltwater outflow as a
 776 constant buoyancy source F , with width L , applied to the bottom of our model domain.



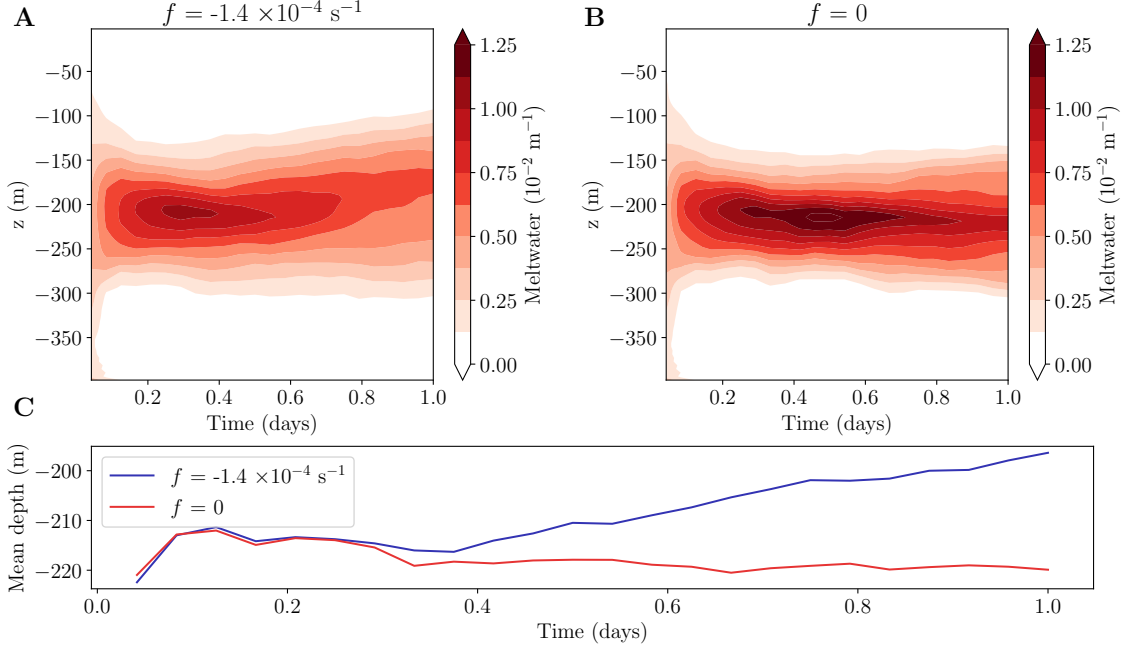
777 FIG. 2. Example solutions of the one-dimensional line plume model for different buoyancy forcings F/L .

778 $h = 0$ represents the base of the ice shelf front. In each case, the black dot highlights the meltwater's settling

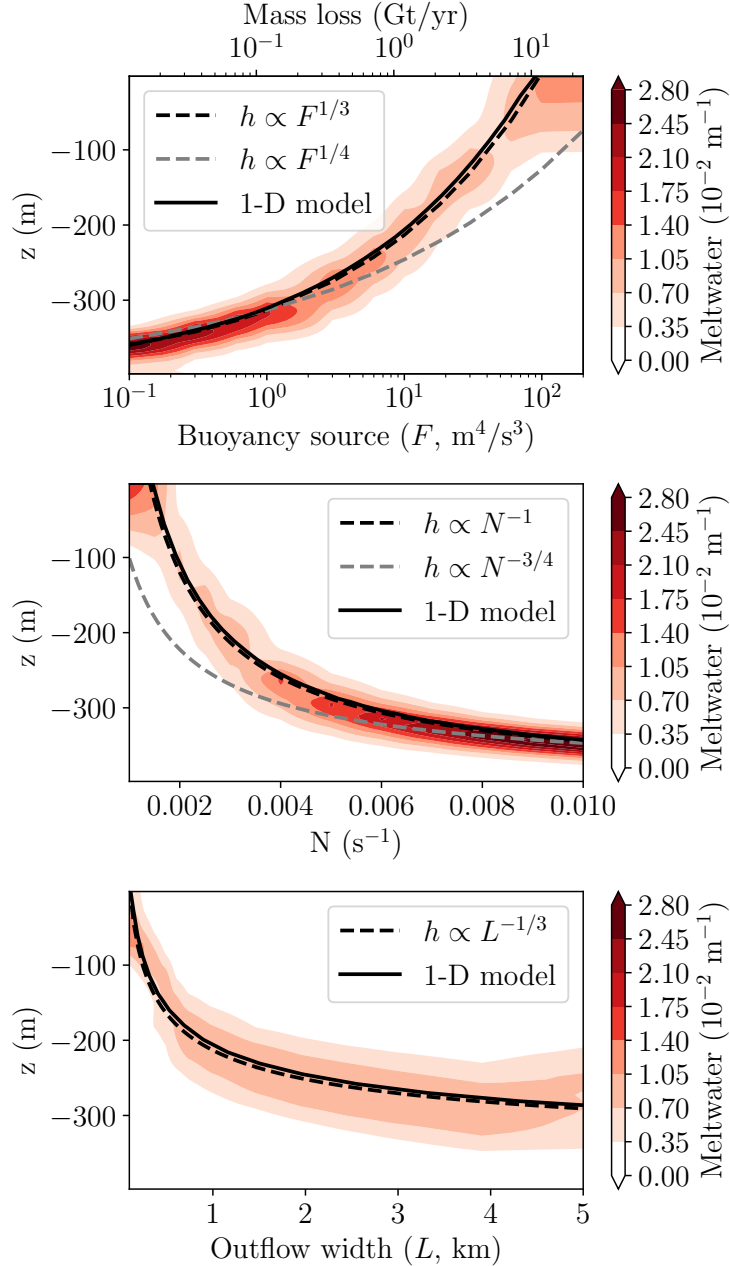
779 depth; this is the level of neutral buoyancy, i.e. where $B(z) = 0$



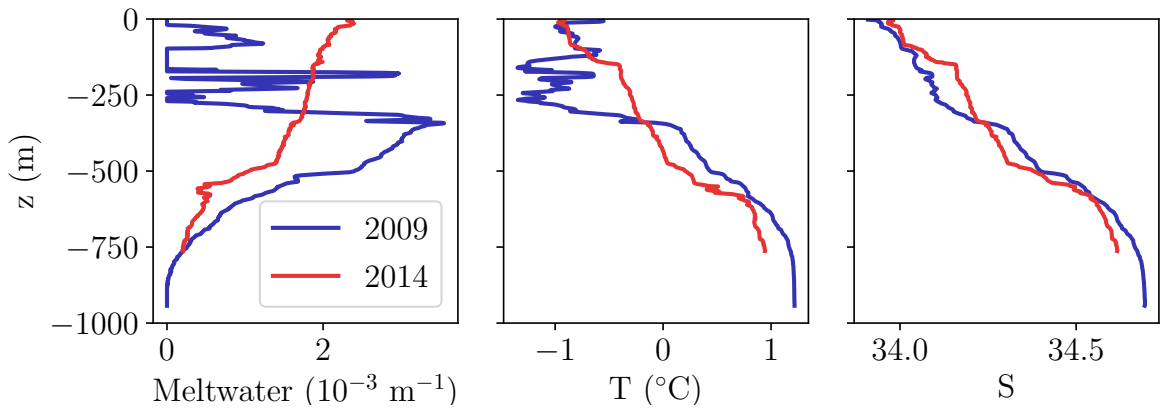
780 FIG. 3. Evolution of a simulated meltwater plume, after 6 hours and after 18 hours. Row A depicts a yz -plane
 781 with $x = 0$ (i.e. perpendicular to the ice shelf front): arrows indicate the flow in this plane, while colors indicate
 782 the flow perpendicular to it. We see the development of a strong zonal flow, consistent with observations of the
 783 outflow from beneath the Pine Island ice shelf. Row B depicts the zonally averaged meltwater distribution, and
 784 row C depicts the meridionally averaged meltwater distribution. Distributions have been normalized to integrate
 785 to 1. The meltwater outflow is deflected to the west by the Coriolis force, and eventually re-enters the domain at
 786 the eastern boundary.



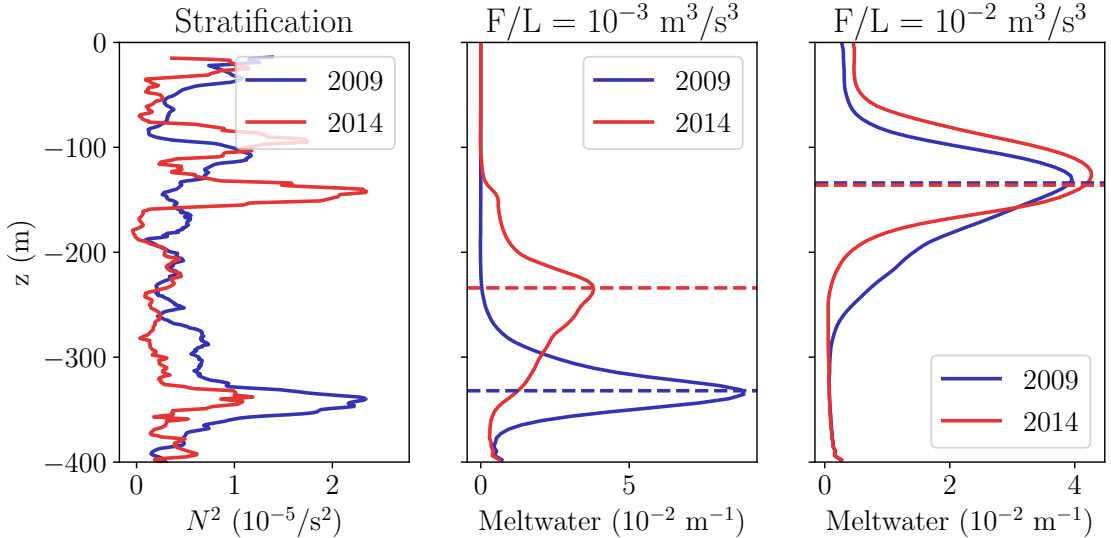
787 FIG. 4. The evolution of the horizontally averaged vertical meltwater distribution over 1 day of simulation,
 788 for a realistic value of the Coriolis parameter f and for a case where $f = 0$. A and B show the evolution of the
 789 distributions, and C shows the evolution of the mean settling depth. Here, $F = 10 \text{ m}^4/\text{s}^3$, and $L = 1 \text{ km}$. In our
 790 simulations, rotational effects broaden the distribution of meltwater over a wider range of depths. The effect on
 791 the mean settling depth is smaller and of the opposite sign as that found by Naveira Garabato et al. (2017); we
 792 discuss this in the text.



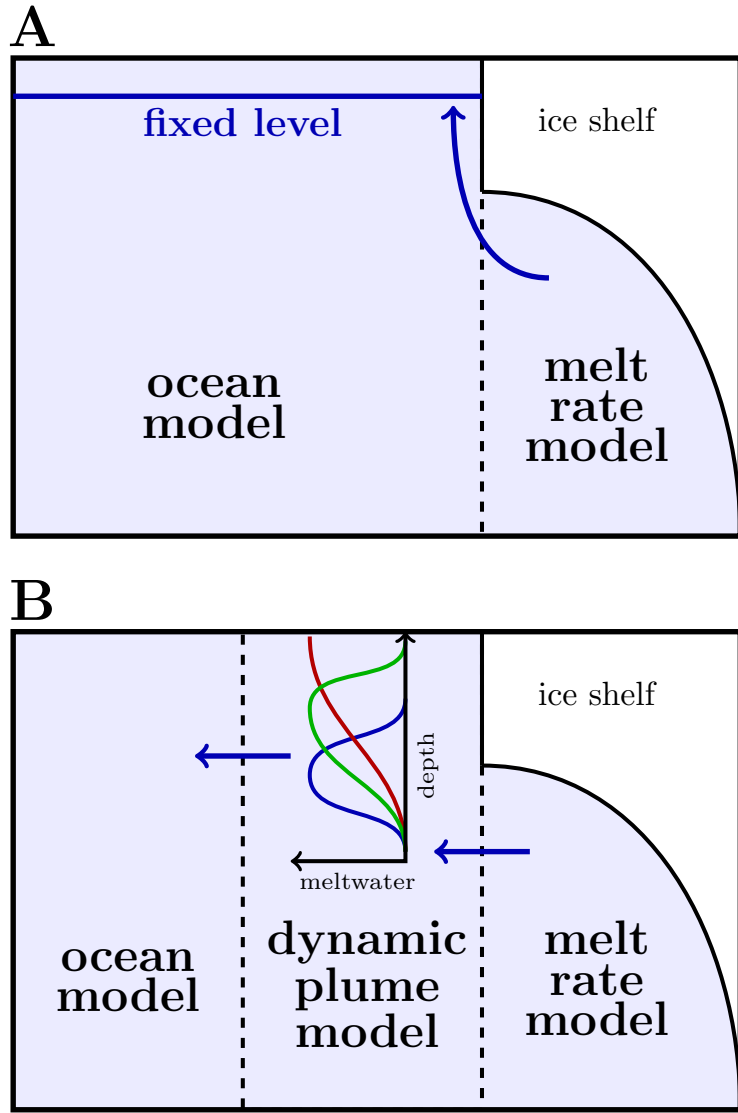
793 FIG. 5. The horizontally averaged vertical meltwater distribution after 6 hours of simulation, for varying
 794 buoyancy source F , varying stratification N , and varying outflow width L . For the case of varying F , we have
 795 also estimated a lower bound on the corresponding mass loss due to melt (see text). On top of the distributions
 796 we plot the settling depths predicted by the simple scaling relationships (dashed) and the one-dimensional line
 797 plume model (solid) with $a = 2.6$: both show excellent agreement with the high-resolution simulations. The
 798 new scaling relationships show substantial improvement over the scaling relationships for point source plumes
 799 ($h \propto (F/N^3)^{1/4}$).



800 FIG. 6. Observed 2009 and 2014 temperature and salinity profiles next to the meltwater outflow from Pine
 801 Island Glacier, as well as estimated meltwater fractions. In 2009, meltwater was primarily centered at a 400m
 802 depth, while in 2014 it was able to rise to the surface.



803 FIG. 7. Simulated vertical meltwater distributions (from LES, solid) for $F/L = 10^{-3} \text{ m}^3/\text{s}^3$ and $F/L = 10^{-2}$
 804 m^3/s^3 , with initial conditions set by observed temperature and salinity profiles for 2009 and 2014. Horizontal
 805 dashed lines indicate the settling depths predicted by the one-dimensional line plume model for the same
 806 conditions; notably, the line plume model accurately predicts the peak of the simulated meltwater distribution in
 807 all cases. We also plot depth profiles of stratification strength in terms of N^2 (see text). For $F/L = 10^{-2} \text{ m}^3/\text{s}^3$
 808 we see that there is little difference in the vertical meltwater distribution between 2009 and 2014 conditions.
 809 However, the simulations with $F/L = 10^{-3} \text{ m}^3/\text{s}^3$ show a marked difference: the qualitative trend is consistent
 810 with observations (Figure 6). Here, we propose that the rising meltwater was “trapped” by the notable local
 811 stratification maximum at around 350m depth in the 2009 conditions.



812 Fig. 8. Schematic describing two different paradigms for Antarctic meltwater fluxes in simulations of global
 813 climate. In paradigm A, the fluxes from a melt rate model are inserted into the ocean model at some fixed vertical
 814 level; this approach has dominated the literature. In paradigm B, the melt rate model is coupled to a dynamic
 815 plume model that describes the small-scale dynamics of buoyant meltwater plumes and accurately calculates the
 816 vertical distribution of meltwater for insertion into the ocean model. Given the potential climatic importance of
 817 glacial meltwater, the strong dependence of settling depth on the buoyancy forcing, and the vast heterogeneity in
 818 the observed mass loss rates and ambient conditions at different ice shelves, this approach would likely represent
 819 a significant improvement over the “one-size-fits-all” approach of paradigm A.

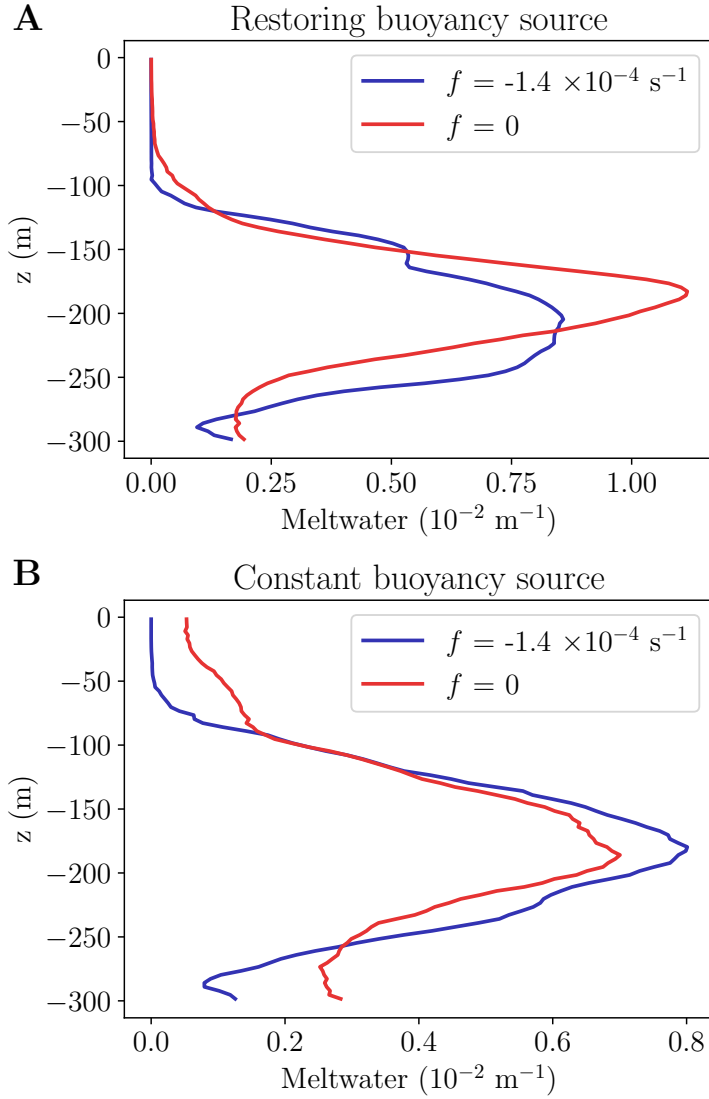


FIG. 9. Vertical meltwater distributions, for rotating and non-rotating cases, in a two-dimensional domain.
 In panel A, we have introduced meltwater via a restoring buoyancy source (following Naveira Garabato et al. (2017), see text), while in panel B we have used a constant buoyancy source (as in the simulations described in the main text). When a constant buoyancy source is employed, the peak of the vertical distribution is not noticeably influenced by the effects of rotation. However, when a restoring buoyancy source is employed, rotation deepens the peak by ~ 50 m, consistent with the simulations of Naveira Garabato et al. (2017). Since the magnitude of the buoyancy source is a primary control on the meltwater's settling depth, the importance of any other parameters can only be accurately investigated by holding the buoyancy source constant; therefore, these results show that the use of restoring non-constant buoyancy sources may exaggerate the effect of rotation on the settling depth.